JOURNAL OF COMPUTATIONAL PHYSICS 13, 569–590 (1973)

A Finite Difference Scheme for Time-Dependent Spherical Radiation Hydrodynamics Problems

JOHN ZINN

University of California, Los Alamos Scientific Laboratory,

Los Alamos, New Mexico 87544

Received October 13, 1972

This paper describes a fast and simple computational procedure for a class of time-dependent radiation transport hydrodynamics problems with spherical symmetry. Local thermodynamic equilibrium is assumed, and effects of time-of-flight retardation of photons are not considered. A two-stream assumption is used wherein the monochromatic intensity function at each given point has one value for directions falling within a prescribed cone and another value for directions outside of that cone. A use of the method is illustrated in a computation of the growth of a nuclear fireball.

INTRODUCTION

This paper describes a computation method designed for time-dependent spherical problems of coupled radiation transport and hydrodynamics in media where the radiative absorption coefficients exhibit strong variations with temperature. The method is based on the assumption that the resultant angular distributions of monochromatic intensities are either (1) approximately isotropic, as in optically thick regions or optically thin regions bounded by optically thick regions or (2) can be approximated by two-valued step functions, as in a cool transparent region outside of an optically thick source.

Local thermodynamic equilibrium is assumed, so that the material internal energy, pressure, and monochromatic absorption coefficients are expressible as functions of local temperature and density. Radiation energy densities and radiation pressures are not included in the equations of state, and photon time-of-flight effects are ignored. These omissions are justified when the time of transit of photons within the volume of physical interest is small compared to the e-folding time for exchange of energy between the matter and the radiation field. With these restrictions the equation of radiative transfer can be written in the form

$$\frac{\partial I_\nu}{\partial s} = \cos\theta \frac{\partial I_\nu}{\partial r} - \frac{\sin\theta}{r} \frac{\partial I_\nu}{\partial \theta} = \mu'(B_\nu - I_\nu), \tag{1}$$

where I_ν is the specific monochromatic intensity at frequency ν in units of energy per unit area per steradian per unit frequency interval per unit time, θ is the angle between the radius vector and the direction of the specified ray, r is the distance from the center of symmetry, μ' is the absorption coefficient corrected for stimulated emission, and B_ν is the Planck function.

The rate of change of material energy per unit volume (omitting hydrodynamic effects for the present) is given by

$$\frac{\partial E_m}{\partial t} = \int_0^\infty \mu' \left(\int_{4\pi} I_\nu \, d\omega - 4\pi B_\nu \right) d\nu, \tag{2}$$

where $d\omega$ is the element of solid angle.

For computing purposes, a quantity of more interest than I_ν itself is the monochromatic flux function,

$$\vec{F}_\nu = 2\pi \int_0^\pi I_\nu(\theta) \sin\theta \cos\theta \, d\theta. \tag{3}$$

$\vec{F}_\nu$ is the integral of the radial component of the intensity function over all solid angles. Equation (3) is appropriate only for systems with planar or spherical symmetry. The element of solid angle is

$$d\omega = 2\pi \sin\theta \, d\theta.$$

In terms of the fluxes the rate of change of material energy per unit volume is

$$\partial E_m/\partial t = -\int_0^\infty \nabla \cdot \vec{F}_\nu \, d\nu + \text{hydrodynamic terms.} \tag{4}$$

This equation is equivalent to Eq. (2).

It is convenient to replace the differential equation of radiative transfer [Eq. (1)] by the equivalent integral equation

$$I_\nu(P_2) = I_\nu(P_1) \exp\left[-\int_{P_1}^{P_2} \mu'(\xi) \, d\xi \right] + \int_{P_1}^{P_2} \mu'(\xi) \, B_\nu(\xi) \exp\left[-\int_\xi^{P_2} \mu'(\xi') \, d\xi' \right] d\xi, \tag{5}$$

where $d\xi$ and $d\xi'$ are elements of distance along the ray connecting points P_1 and P_2.

With the inclusion of fluid motions, the coupled equations to be solved are

$$\partial\rho/\partial t = -\nabla \cdot (\rho\vec{v}), \qquad \text{(cons. of mass)} \tag{6}$$

$$\partial(\rho v_\alpha)/\partial t = -\nabla \cdot (\rho v_\alpha \vec{v}) - \nabla_\alpha P, \qquad \text{(cons. of momentum)} \tag{7}$$

and

$$\partial E_m/\partial t = -\nabla \cdot (E_m \vec{v}) - P\nabla \cdot \vec{v} - \int_0^\infty \nabla \cdot \vec{F}_\nu \, d\nu, \qquad \text{(cons. of energy)} \tag{8}$$

together with the transport equation (5). The set is closed upon specification of the equation of state relations

$$P = P(\rho, E_m), \qquad T = T(\rho, E_m), \tag{9}$$

the radiative absorption coefficients

$$\mu' = \mu'(\rho, E_m, \nu) \tag{10}$$

and definitions of the flux [Eq. (3)] and the Planck function.

In Eqs. (6)–(10), quantities not previously defined are the mass density ρ, the pressure P, the temperature T, the velocity $\vec{v}$, and the αth component of velocity v_α.

Finite Difference Approximations

A. *Radiation Transport*

We shall represent the physical system by an array of J concentric volume elements (spherical shells) and assume that the density, temperature, and other intensive quantities are spatially uniform within each volume element. Then if two points P_1 and P_2 are on the surface (or surfaces) of a volume element and the distance between the points is Δs, the monochromatic intensity at P_2 along the direction of a ray from P_1 to P_2 is

$$I_\nu(P_2) = I_\nu(P_1)\, e^{-\mu' \Delta s} + B_\nu(1 - e^{-\mu' \Delta s}), \tag{11}$$

where μ' and B_ν are the values existing at the given instant in the given volume element.

The radiation fluxes F_ν will be defined at the cell boundaries (shell surfaces). The flux at each boundary will be computed as the difference between an outward-going flux,

$$F_\nu^+ = 2\pi \int_0^{\pi/2} I_\nu(\theta) \sin\theta \cos\theta \, d\theta, \tag{12}$$

and an inward-going flux

$$F_\nu^- = -2\pi \int_{\pi/2}^{\pi} I_\nu(\theta) \sin\theta \cos\theta \, d\theta. \tag{13}$$

Henceforth, until otherwise mentioned, we shall drop the subscript ν, remembering that we will actually calculate the flux in each of a large number of frequency bands.

Now, let R_1 and R_2 refer, respectively, to the inner and outer radii of a given cell, and let θ_1 and θ_2 be the values of θ for a given ray measured at R_1 and R_2, respectively. (Note that θ_1 and θ_2 are related via $R_1 \sin\theta_1 = R_2 \sin\theta_2$.) Let $I_1(\theta_1)$ and $I_2(\theta_2)$ be the intensity of a given ray at locations R_1 and R_2, and let $\Delta s(\theta_2)$ be the distance between surfaces R_1 and R_2 measured along the path of the ray. Furthermore, let

$$\theta_m \equiv \arcsin(R_1/R_2), \tag{14}$$

the maximum value of θ_2 for rays that pass through the surface R_1. Then according to Eqs. (11)–(13), the outward flux at R_2 is

$$\begin{aligned} F_2^+ = {} & 2\pi \int_0^{\theta_m} I_1(\theta_1)\, e^{-\mu' \Delta s(\theta_2)} \sin\theta_2 \cos\theta_2 \, d\theta_2 \\ & + B\left[\pi \sin^2\theta_m - 2\pi \int_0^{\theta_m} e^{-\mu' \Delta s(\theta_2)} \sin\theta_2 \cos\theta_2 \, d\theta_2\right] \\ & + 2\pi \int_{\theta_m}^{\pi/2} I_2(\pi - \theta_2)\, e^{-\mu' \Delta s(\theta_2)} \sin\theta_2 \cos\theta_2 \, d\theta_2 \\ & + B\left[\pi \cos^2\theta_m - 2\pi \int_{\theta_m}^{\pi/2} e^{-\mu' \Delta s(\theta_2)} \sin\theta_2 \cos\theta_2 \, d\theta_2\right]. \end{aligned} \tag{15}$$

The first two terms arise from rays passing through both R_1 and R_2, while the latter two terms account for those rays which pass through R_2 in the inward direction and reemerge through R_2 without intersecting R_1.

The inward flux at R_1 is

$$\begin{aligned} F_1^- = {} & \frac{2\pi}{\sin^2\theta_m} \int_0^{\theta_m} I_2(\pi - \theta_2)\, e^{-\mu' \Delta s(\theta_2)} \sin\theta_2 \cos\theta_2 \, d\theta_2 \\ & + \pi B\left[1 - \frac{2}{\sin^2\theta_m} \int_0^{\theta_m} e^{-\mu' \Delta s(\theta_2)} \sin\theta_2 \cos\theta_2 \, d\theta_2\right]. \end{aligned} \tag{16}$$

Now for $0 \leqslant \theta_2 < \theta_m$

$$\Delta s(\theta_2) \equiv \Delta s_1(\theta_2) = R_2 \cos\theta_2 - (R_1^2 - R_2^2 \sin^2\theta_2)^{1/2}, \tag{17}$$

and for $\theta_m < \theta_2 \leqslant (\pi/2)$

$$\Delta s(\theta_2) \equiv \Delta s_2(\theta_2) = 2R_2 \cos \theta_2 . \tag{18}$$

Next we assume that at each point in space the monochromatic intensity distribution can be approximated by a two-valued step function. The intensity I has either of two values I_a or I_b, respectively, depending on whether the ray direction, θ, $(0 \leqslant \theta \leqslant \pi)$ is greater than or smaller than a specified value θ_s. θ_s is intended to represent the half-angle subtended at a given location by the principal radiating source. Thus, for example, at points exterior to a hot optically thick source, θ_s would be the half-angle subtended by the source; then the intensities would be large for angles $\theta \leqslant \theta_s$ and very small for $\theta_s \leqslant \theta \leqslant \pi$ (see Fig. 1). The effective

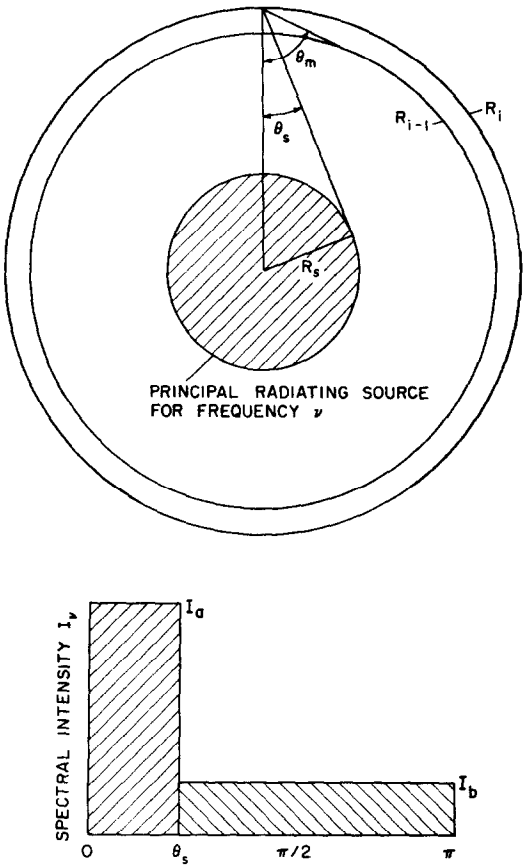

FIG. 1. Diagrams of the assumed geometry and the angular distribution of intensity.

source radius R_s can be determined at each time step for each frequency group, and it is generally taken to be the radius at which the optical depth is unity. Then at a given mesh boundary with radius R_i, the value of θ_s is

$$\theta_s = \arcsin (R_s/R_i), \tag{19}$$

provided that $R_i > R_s$. Inside the source the intensity is assumed to be isotropic; accordingly, when $R_i \leqslant R_s$, θ_s is set equal either to $\pi/2$ or to

$$\theta_m = \arcsin (R_{i-1}/R_i). \tag{20}$$

The above choice will be clarified in Eqs. (21) and (22).

With the asumption that the monochromatic intensities at each mesh boundary are isotropic within angles $0 \leqslant \theta \leqslant \theta_s$ (or within θ_m or $\pi/2$ in the event that $R_i \leqslant R_s$) with one value I_a, and again isotropic with a different value I_b for $\theta_s \leqslant \theta \leqslant \pi$, the entire array of fluxes can be generated in two passes (one inward and one outward) through the mesh.

This assumed intensity distribution is exact in two kinds of limiting cases: (1) within an optically thick region of uniform temperature, where I does not depend on θ (and then $I_a = I_b$), and (2) in a vacuum outside of a uniformly emitting sphere, or in an evacuated spherical shell between uniformly emitting surfaces.

Now consider a mesh cell bounded by surfaces of radii R_1 and R_2, respectively. Assume that the effective source radius R_s has been determined and define

$$\theta_{1s} = \begin{cases} \arcsin(R_s/R_1) & \text{for } R_1 \geqslant R_s, \\ \pi/2 & \text{for } R_1 \leqslant R_s, \end{cases} \tag{21}$$

and

$$\theta_{2s} = \begin{cases} \arcsin(R_s/R_2) & \text{for } R_1 \geqslant R_s, \\ \theta_m & \text{for } R_1 \leqslant R_s. \end{cases} \tag{22}$$

Let the inward and outward flux components at surface R_1 be F_1^- and F_1^+, and let the corresponding fluxes at R_2 be F_2^- and F_2^+. Then with the assumed I vs θ relationships the four flux components are related by the coupled equations,

$$\begin{aligned} F_1^+ &= 2\pi I_{1a} \int_0^{\theta_{1s}} \sin\theta \cos\theta \, d\theta + 2\pi I_{1b} \int_{\theta_{1s}}^{\pi/2} \sin\theta \cos\theta \, d\theta \\ &= \pi I_{1a} \sin^2 \theta_{1s} + \pi I_{1b}(1 - \sin^2 \theta_{1s}), \end{aligned} \tag{23}$$

$$F_2^- = -2\pi I_{2b} \int_{\pi/2}^{\pi} \sin\theta \cos\theta \, d\theta = \pi I_{2b}, \tag{24}$$

$$F_2^+ = \pi I_{2a} \sin^2 \theta_{2s} + \pi I_{2b}(1 - \sin^2 \theta_{2s}), \tag{25}$$

and

$$F_1^- = \pi I_{1b}\,, \tag{26}$$

together with Eqs. (15) and (16).

The integrals in Eqs. (15) and (16) are all either of the form

$$\int_{\theta_A}^{\theta_B} \sin\theta\cos\theta\, e^{-\mu'\Delta s_1(\theta)}\, d\theta,$$

with $\Delta s_1(\theta)$ given by Eq. (17), or of the form

$$\int_{\theta_m}^{\pi/2} \sin\theta\cos\theta\, e^{-\mu'\Delta s_2(\theta)}\, d\theta,$$

with $\Delta s_2(\theta)$ given by Eq. (18). Both can be integrated in closed form.

Let

$$\begin{aligned}
&\Delta R \equiv R_2 - R_1\,, \qquad \tau \equiv \mu'\Delta R,\\
&u(\theta) = (\tau/\Delta R)(R_2\cos\theta - (R_1^2 - R_2\sin^2\theta)^{1/2}),\\
&u_A \equiv u(\theta_A), \qquad u_B \equiv u(\theta_B),\\
&u_s \equiv u(\theta_{2s}) = (\tau/\Delta R)((R_2^2 - R_s^2)^{1/2} - (R_1^2 - R_s^2)^{1/2}),\\
&u_m \equiv u(\theta_m) = \tau((R_1 + R_2)/(R_2 - R_1))^{1/2},
\end{aligned} \tag{27}$$

$$G(u) \equiv e^{-u}\left(\frac{1}{u^2} - \frac{1}{u}\right) + \int_u^\infty \frac{e^{-x}}{x}\, dx, \tag{28}$$

and

$$H(u) \equiv e^{-u}(1 + u). \tag{29}$$

In terms of these functions,

$$\int_{\theta_A}^{\theta_B} \sin\theta\cos\theta\, e^{-\mu'\Delta s_1(\theta)}\, d\theta = \frac{(R_1 + R_2)^2\,\tau^2}{8R_2^2}\{G(u_A) - G(u_B)\} - \frac{(R_2 - R_1)^2}{4R_2^2\tau^2}\{H(u_A) - H(u_B)\},$$

and

$$\int_{\theta_m}^{\pi/2} \sin\theta\cos\theta\, e^{-\mu'\Delta s_2(\theta)}\, d\theta = \frac{(R_2 - R_1)^2}{4R_2^2\tau^2}\{1 - H(2u_m)\}.$$

Then the results of integrating Eqs. (15) and (16) can be expressed in the form

$$F_2^+ = \pi I_{1a}\left[\frac{(R_1+R_2)^2\tau^2}{4R_2^2}\{G(\tau)-G(u_s)\}-\frac{(R_2-R_1)^2}{2R_2^2\tau^2}\{H(\tau)-H(u_s)\}\right]$$
$$+\pi I_{1b}\left[\frac{(R_1+R_2)^2\tau^2}{4R_2^2}\{G(u_s)-G(u_m)\}-\frac{(R_2-R_1)^2}{2R_2^2\tau^2}\{H(u_s)-H(u_m)\}\right]$$
$$+\pi I_{2b}\left[\frac{(R_2-R_1)^2}{2R_2^2\tau^2}\{1-H(2u_m)\}\right]$$
$$+\pi B\left[1-\frac{(R_1+R_2)^2\tau^2}{4R_2^2}\{G(\tau)-G(u_m)\}\right.$$
$$\left.-\frac{(R_2-R_1)^2}{2R_2^2\tau^2}\{1-H(\tau)+H(u_m)-H(2u_m)\}\right], \tag{30}$$

and

$$F_1^- = \pi B+\pi(I_{2b}-B)\left[\frac{(R_1+R_2)^2\tau^2}{4R_1^2}\{G(\tau)-G(u_m)\}\right.$$
$$\left.-\frac{(R_2-R_1)^2}{2R_1^2\tau^2}\{H(\tau)-H(u_m)\}\right]. \tag{31}$$

Equations (23)–(26), (30), and (31) constitute a set of six coupled equations connecting the flux components F_1^+, F_1^-, F_2^+, and F_2^- and the intensities I_{1a}, I_{1b}, I_{2a}, and I_{2b}. The six can be combined so as to eliminate the intensities. The combined equations are

$$F_1^- = \pi B+(F_2^- -\pi B)\left[\frac{(R_1+R_2)^2\tau^2}{4R_1^2}\{G(\tau)-G(u_m)\}\right.$$
$$\left.-\frac{(R_2-R_1)^2}{2R_1^2\tau^2}\{H(\tau)-H(u_m)\}\right], \tag{32}$$

and

$$F_2^+ = \pi B+\frac{(R_1+R_2)^2\tau^2}{4R_2^2}\left[\left(\frac{F_1^+-F_1^-}{\sin^2\theta_{1s}}\right)\{G(\tau)-G(u_s)\}\right.$$
$$\left.+(F_1^- -\pi B)\{G(u_s)-G(u_m)\}\right]$$
$$+\frac{(R_2-R_1)^2}{2R_2^2\tau^2}\left[(F_2^- -\pi B)\{1-H(2u_m)\}\right.$$
$$\left.-\left(\frac{F_1^+-F_1^-}{\sin^2\theta_{1s}}\right)\{H(\tau)-H(u_s)\}-(F_1^- -\pi B)\{H(u_s)-H(u_m)\}\right]. \tag{33}$$

Inside the source region—i.e., where $R_1 \leqslant R_s$, we take $\theta_{1s} = \pi/2$ and $\theta_{2s} = \theta_m$ [cf. Eqs. (21) and (22)]; then Eq. (33) reduces to the simpler form

$$F_2^+ = \pi B + (F_1^- - \pi B)\left[\frac{(R_1 + R_2)^2\,\tau^2}{4R_2^2}\{G(\tau) - G(u_m)\}\right.$$
$$\left. - \frac{(R_2 - R_1)^2}{2R_2^2\tau^2}\{H(\tau) - H(u_m)\}\right]$$
$$+ (F_2^- - \pi B)\left\{\frac{(R_2 - R_1)^2}{2R_2^2\tau^2}\right\}\{1 - H(2u_m)\}. \tag{34}$$

Equations (32) and (33) [or (34)] form the basis of the finite difference scheme. For each frequency group (subscript ν) and for each mesh cell (subscript i) one needs to find the four quantities $F^+_{1,i,\nu}$, $F^-_{1,i,\nu}$, $F^+_{2,i,\nu}$, and $F^-_{2,i,\nu}$. Equations (32) and (33) [or (34)], together with the flux continuity conditions

$$F^+_{1,i+1,\nu} = F^+_{2,i,\nu} \tag{35}$$

and

$$F^-_{1,i+1,\nu} = F^-_{2,i,\nu}, \tag{36}$$

constitute the necessary set of four equations. Equation (32) gives the inward flux through the inner surface of a cell in terms of the inward flux through the outer surface and the properties of the medium in the cell. Thus, starting with a known inward flux through the outermost mesh boundary (generally zero), the complete array of inward fluxes can be generated with Eqs. (32) and (36). Equation (33) or (34) gives the outward flux at each boundary in terms of the outward flux through the previous boundary, the inward flux through both boundaries, and the properties of the medium in between. Thus, given the array of inward fluxes already computed, and starting with $F_1^+ = 0$ at the center of symmetry, the complete array of outward fluxes can be generated. The process is repeated for each frequency group.

From Eq. (4) the rate of change of energy per unit volume in the ith cell is

$$(\partial E/\partial t)_i = \left[-\frac{3}{(R_2^3 - R_1^3)}\int_0^\infty \{R_1^2(F_1^+ - F_1^-) - R_2^2(F_2^+ - F_2^-)\}\,d\nu\right]_i$$
$$+ \text{hydrodynamic terms.} \tag{37}$$

The integration over frequency is replaced in practice by a simple summation of contributions from each of a number of frequency groups. The hydrodynamic terms in Eq. (37) are computed separately (see Section B) and added linearly.

Special provision must be made for situations where part of the system is

optically thick in one or more frequency groups. In computing the flux at a boundary between two optically thick cells, (i.e., thick at frequency ν), application of Eqs. (32)–(36) would give

$$F_{i,\nu} = \pi(B_{i-\frac{1}{2}} - B_{i+\frac{1}{2}})_\nu . \tag{38}$$

This would be the correct expression for the boundary flux if the temperature profile did actually consist of a series of isothermal zones. If, however, the temperature profile were continuous, the flux would be represented better by the diffusion approximation

$$F_\nu = -\tfrac{4}{3}\pi\nabla B_\nu/\mu'. \tag{39}$$

The simplest finite difference representation of Eq. (39) for the flux at the ith boundary is

$$F_i = 8/3\pi(B_{i-\frac{1}{2}} - B_{i+\frac{1}{2}})/(\tau_{i-\frac{1}{2}} + \tau_{i+\frac{1}{2}}) \tag{40}$$

(subscript ν suppressed).

Equation (40) is used in place of Eqs. (32)–(36) whenever both $\tau_{i-\frac{1}{2}}$ and $\tau_{i+\frac{1}{2}}$ are greater than 2.0.

When only one of a pair of adjacent cells is optically thick, no special action is necessary, as Eqs. (32)–(36) give a reasonable result.

With the rates of change of specific internal energy due to radiation transport given by Eq. (37) (without the hydrodynamic terms), the computational time step is chosen so that the fractional energy change in a time step does not exceed a specified limit f (say 0.1) anywhere in the mesh. That is

$$\Delta t = f \min \left\{ E_i \Big/ \left(\frac{\partial E}{\partial t}\right)_i \right\}. \tag{41}$$

When most of the energy transfer occurs in frequency groups which are not optically thick, it is found that a small value of f can be used without making Δt inconveniently small. When this is the case no serious time-centering problems arise. The computer code based on this difference scheme (cf. next section) is in fact not time-centered.

This method is not advantageous for problems that are dominated by radiation diffusion (as contrasted with radiation transport). With fluxes computed via Eq. (40) the time steps given by (41) tend to be inconveniently small.

B. *Hydrodynamics*

The radiation transport procedure is not restricted to a particular distribution of mesh cell thicknesses; therefore, it can be combined equally well with either an

Eulerian or Lagrangian hydrodynamics scheme. For the particular set of problems at hand an explicit Lagrangian method was used [1].

The hydrodynamic calculations are performed in parallel with the transport calculations, and either one or an integral number of hydrodynamic time steps are taken per radiation time step.

The hydrodynamic equations (6)–(8), as specialized to a system with spherical symmetry, are represented in finite difference form as follows: Given a time increment Δt_H equal to or shorter than the limiting increment allowed by Courant conditions, and given a set of values of m_i ($i = 1,..., J$), the masses of fluid in each of the J mesh cells, one updates the hydrodynamic quantities from time t to $t + \Delta t_H$ in three steps.

In step I the pressure P_i and viscous pressure Q_i are computed for each mesh cell. P_i is computed with the density ρ_i and internal energy per unit mass I_i together with the given equation of state. Q_i is set equal to zero in zones that are expanding. Otherwise it is given by the expression

$$Q_i = \alpha P_i \Delta V_i / c_i \Delta t_H \{R_{i-\frac{1}{2}}^2 + R_{i+\frac{1}{2}}^2\}, \tag{42}$$

where ΔV_i is the cell volume change occurring in the previous time step, c_i is the local sound speed, and α is a constant of order 0.1–1. Indices $i - \frac{1}{2}$ and $i + \frac{1}{2}$ refer to the cell boundaries.

In step II the acceleration $a_{i+\frac{1}{2}}$ of each boundary and the displacement of each boundary $\Delta R_{i+\frac{1}{2}}$ in time Δt_H is computed. The internal energy per unit mass I_i in each cell and the radius $R_{i+\frac{1}{2}}$ and velocity $v_{i+\frac{1}{2}}$ of each boundary are updated to $t + \Delta t_H$. The difference equations, to be applied in sequential order, are

$$a_{i+\frac{1}{2}} = 8\pi R_{i+\frac{1}{2}}^2 (P_i + Q_i - P_{i+1} - Q_{i+1})/(m_i + m_{i+1}), \tag{43}$$

$$\Delta R_{i+\frac{1}{2}} = \Delta t_H (v_{i+\frac{1}{2}} + \tfrac{1}{2} a_{i+\frac{1}{2}} \Delta t_H), \tag{44}$$

$$I_i = I_i + 4\pi (P_i + Q_i)(R_{i-\frac{1}{2}}^2 \Delta R_{i-\frac{1}{2}} - R_{i+\frac{1}{2}}^2 \Delta R_{i+\frac{1}{2}})/m_i, \tag{45}$$

$$v_{i+\frac{1}{2}} = v_{i+\frac{1}{2}} + a_{i+\frac{1}{2}} \Delta t_H, \tag{46}$$

and

$$R_{i+\frac{1}{2}} = R_{i+\frac{1}{2}} + \Delta R_{i+\frac{1}{2}}. \tag{47}$$

The final cell volumes V_i and mass densities ρ_i are computed in step III by the formulae

$$V_i = \tfrac{4}{3}\pi (R_{i+\frac{1}{2}}^3 - R_{i-\frac{1}{2}}^3) \tag{48}$$

and

$$\rho_i = m_i / V_i. \tag{49}$$

The hydrodynamic time step is equal to the radiation time step from Eq. (41) divided by an integer. That is,

$$\Delta t_H = \Delta t/n, \qquad n = 1, 2,.... \tag{50}$$

The integer n is chosen so that Δt_H is equal to or smaller than the largest Δt allowed by the Courant conditions. At the end of each hydrodynamic time step the specific internal energies I_i are updated with the $(\partial E/\partial t)_i$ computed via Eq. (37) at the beginning of the radiation time step Δt. That is

$$I_i = I_i + \Delta t_H(\partial E/\partial t)_{\mathrm{Rad},i}/m_i\,. \tag{51}$$

C. *Limiting Cases and Accuracy of the Approximations*

Equations (32)–(36) have the necessary property that when $\tau = 0$,

$$R_1^2(F_1^+ - F_1^-) = R_2^2(F_2^+ - F_2^-),$$

so that $\nabla \cdot F = 0$.

It is also necessary that if $R_s \ll R_2$ and $F_2^- = B = 0$, then

$$R_2F_2^+ = R_1^2F_1^+e^{-\tau}.$$

Equations (32) and (33) do in fact give this result.

Another important limiting case is that of an optically thin cell with no fluxes incident on it. To first order in τ, the radiation emitted by such a cell should be

$$4\pi R_2^2F_2^+ = 16/3\pi^2\tau B(R_1^2 + R_1R_2 + R_2^2).$$

Equations (32) and (34) do give this result.

In the systems for which this method was developed, μ' is found to vary over ten powers of ten for the range of frequencies and temperatures of physical interest. That is, τ is usually either much smaller than one or much greater. In both limits the present approximations are nearly exact. The computed flux distributions are sensitive to the assumed angular distribution of intensity only in those relatively rare cases where the local τ values are close to one.

Since the results are largely insensitive to the assumed angular distribution of $I(\theta)$, the method used for estimating the "source radius" R_s is not critical. If the temperature decreases in the outward direction and the absorption coefficients are strongly increasing functions of temperature, then the central region will tend to be optically thick out to a certain radius and thin at larger radii, and the actual shape of the $I(\theta)$ vs θ distribution will be close to a step function: The effective R_s will be close to the radius at which the optical depth $\int_R^\infty \mu' dr$ is equal to 1. On the other hand, if the absorption coefficients decrease strongly with increasing temperature,

the intensities will be close to isotropic (though with a wide range of magnitude) everywhere in the system. In such cases R_s will be chosen as the outer boundary of the mesh.

The present method, through its simplified treatment of the angular intensity

overall accuracy and requirements on computer time.

The legitimacy of our neglect of radiation pressure and radiation energy density depends, of course, on the problem. This method was developed for a class of problems similar to that described in the next section—on the growth of a nuclear fireball in air at sea level. In sea level air the radiation energy is smaller than the material energy only at temperatures below 200 eV. Temperatures above 200 eV do occur within the first few tenth-microseconds, and our neglect of radiation energy makes the computation inaccurate for this period of time. The principal effect of the omission is to produce a timing error of order 10^{-7} sec. In air at lower densities the radiation energy would be important well below 200 eV if the radiation field reached local thermodynamic equilibrium; however, at low densities fireball dimensions tend to be smaller than relevant radiation mean free paths, and the radiation energy density does not reach L.T.E. Consistent with our neglect of radiation pressure, we have also neglected photon times-of-flight (retardation). This would not be justified if we were interested in effects occurring on time scales comparable with photon flight times and/or very early times when radiation pressure and energy density are important. Retardation is not important in fireballs at times later than 1 μsec.

Scattering of photons is also not considered. Thompson scattering begins to be an important physical effect at photon energies of 20 keV, and neglect of scattering makes the present treatment inaccurate at higher energies. For most fireball problems, however, the fraction of photons above 20 keV is very small. The neglect of molecular resonance scattering is probably more serious. Molecular scattering does appear to have an observable effect on fireball profiles near "minimum time" (defined in the next section).

Computation of Growth of a Nuclear Fireball

The present computational scheme was developed for problems of nuclear fireball growth. It has been in use at Los Alamos and elsewhere since 1964 for problems of this sort.

The physical problem, which has been described many times previously (see Refs. [2]–[7]), is as follows: Close to the bomb the air is heated initially to temperatures approaching 10^7 K. This hot region then expands by radiation transport and

by hydrodynamics. The physical system includes regions with temperatures ranging from ambient to 10^7 K and air densities between about 10^{-5} and 10^2 g/cm^3. The radiation transport problem includes photons with energies between 10^{-1} and 10^5 eV.

The computer code includes tables of equation of state data P and T vs ρ and E, tables of radiative absorption coefficients μ' vs ρ, E, and ν, and tables of Planck function integrals $\int_{\nu_{1i}}^{\nu_{2i}} B_\nu d\nu$ vs T and ν. (The frequency spectrum is discretized, the ith group being bounded by frequencies ν_{1i} and ν_{2i}. Forty frequency groups are used.) The equation of state and absorption coefficient data are derived primarily from Refs. [8]–[11]. Absorption coefficients (local Rosseland means) for normal density air at a few representative temperatures are plotted vs photon energy in Fig. 2.

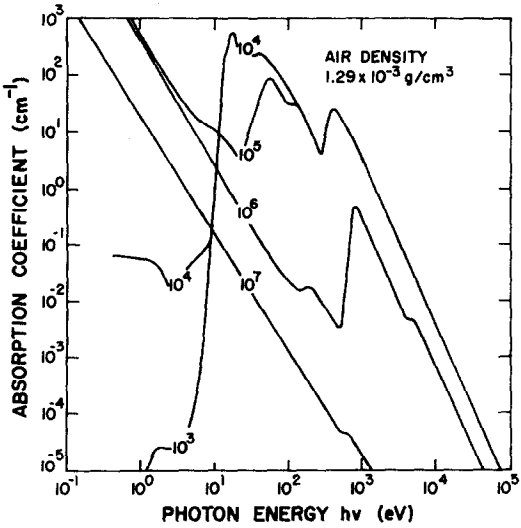

FIG. 2. Plots of radiative absorption coefficients of ambient density air vs photon energy at five different temperatures.

Output of the code includes computer-generated profiles of visible radiance (W/cm^2sr) vs radius across the fireball disc as well as radiant power (W/cm^2) in several wave length bands. (These are generated in a separate subroutine which computes the angular distribution of visible radiation in detail.) The code also plots profiles of density and temperature vs radius from the burst point.

The source (of mass M) is placed in the first Lagrangian zone and its temperature is held constant for a specified period of time τ_x. The temperature T is so chosen that the sum of 1, the energy radiated from the surface area of the zone A at the

rate σT^4 in the time τ_x, plus 2, the material energy in the mass M at temperature T, add up to the yield Y.

Let us assume that $Y = 1Mt$ (4.18×10^{22} ergs). We shall assume also that $M = 10^6$ g, $A = 10^5$ cm^2, $\tau_x = 10^{-7}$ sec. Taking specific heat to be 2×10^8 erg/g °K, we then obtain a temperature $T = 1.8 \times 10^7$ K (1.6 keV). The peak of the blackbody spectral distribution for this temperature occurs in the soft X-ray region at $h\nu = 4.5$ keV. In the computation the radiation is emitted from the zone in stepwise fashion with time steps limited by Eq. (41).

The first X-rays are absorbed in cells close to the origin. The temperature in these innermost cells rises as a result to a value such that the air atoms are stripped of electrons, and their X-ray absorption coefficients drop sharply (see Fig. 2). Subsequent X-ray photons are transmitted by the inner cells and absorbed in cooler cells farther out. The latter are heated in turn until they, too, become transparent. The process continues until, at the end of the X-ray emission phase, the air temperature profile consists of a quasiisothermal sphere with a sharp boundary. Outside the isothermal sphere is a region of exponentially decreasing temperature created by the harder X-rays in the original Planck distribution.

Optical absorption coefficients of air in the temperature range between 300 and 20 000 K rise rapidly with increasing temperature (Fig. 2), and for the distance scales of the present problem, the air is effectively opaque at temperatures above 8000 K. The region outside of the isothermal sphere has temperatures exceeding 8000 K, so that it conceals the much hotter isothermal sphere. A set of temperature, density, and brightness plots for $t = 10^{-6}$ sec are in Fig. 3. The visual fireball radius at that time is the radius where the temperature is 8000 K.

For about 100 μsec the isothermal sphere grows by radiation transport. The radiation emitted in the interior consists predominantly of photons with energies between the air L and K absorption edges (vacuum ultraviolet). For temperatures between 10^4 and 10^6 K the air absorption coefficients in the vacuum UV decrease with increasing temperature owing to depopulation of the L shell. Photons emitted in the isothermal sphere have long mean free paths until they reach the surface where the air is cold. The process of emission within the isothermal sphere and absorption at the surface produces a rapid expansion of the region. The flat temperature profile is preserved while the average temperature drops. The velocity of the front decreases with the average temperature. The absorbing region outside of the isothermal sphere remains stationary, while the isothermal sphere grows through it. When the hot region passes across the 8000 K radius, the observable optical emission increases sharply. Temperature, density, and brightness profiles for $t = 5 \times 10^{-5}$ sec are in Fig. 4. They show a strong shock driven by the expanding bomb vapor and a second, much weaker, shock at the front of the radiatively expanding fireball,

As the fireball temperature drops, a condition is reached ($T \approx 500\,000$ K)

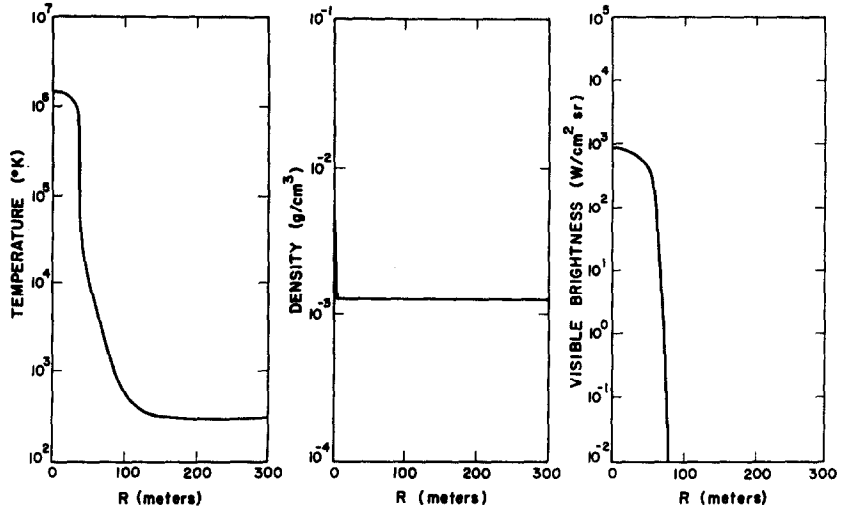

FIG. 3. Profiles of temperature, density, and visible brightness for $t = 1 \times 10^{-6}$ sec.

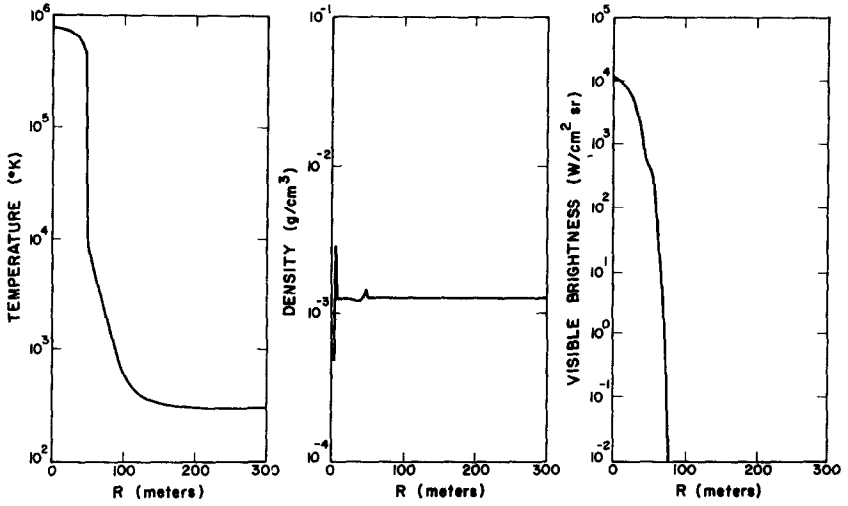

FIG. 4. Profiles of temperature, density, and visible brightness for $t = 5 \times 10^{-5}$ sec.

where the radiative expansion speed is no longer large compared to the sound speed. A strong shock wave forms and subsequent expansion of the fireball is dominated by hydrodynamics. Profiles for $t = 3 \times 10^{-4}$ sec in Fig. 5 show a fully developed fireball shock. The inner shock has largely disappeared.

As the expansion continues the shock strength decreases. Its surface brightness drops while its surface area increases. The net optical power output increases to a maximum at 10^{-3} sec and then decreases. Total observable optical power is plotted vs time in Fig. 6.

The shocked air is opaque and conceals the hotter region inside, remnant of the isothermal sphere. As the shock temperature drops, however, its opacity decreases

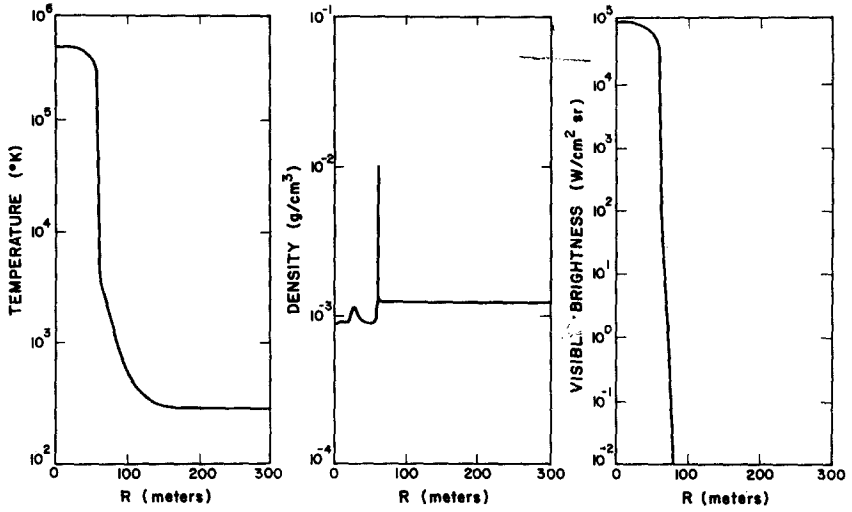

FIG. 5. Profiles of temperature, density, and visible brightness for $t = 3 \times 10^{-4}$ sec.

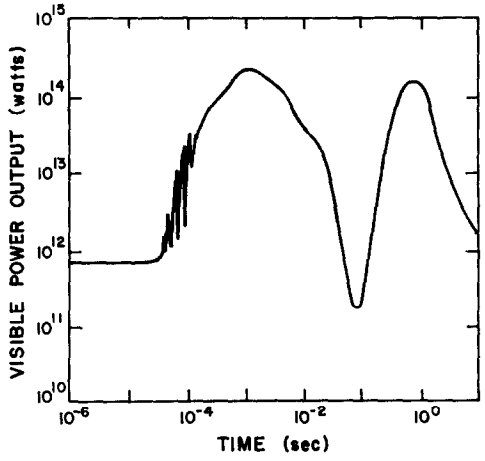

FIG. 6. Computed optical power vs time.

until, at 9×10^{-2} sec, transmitted light from the isothermal sphere begins to predominate over light emitted by the shock itself. The net optical output at this point is a minimum. Further expansion produces further transparency of the shock, and the optical power increases (Fig. 6). Profiles of temperature, density, and brightness at 9×10^{-2} sec are shown in Fig. 7.

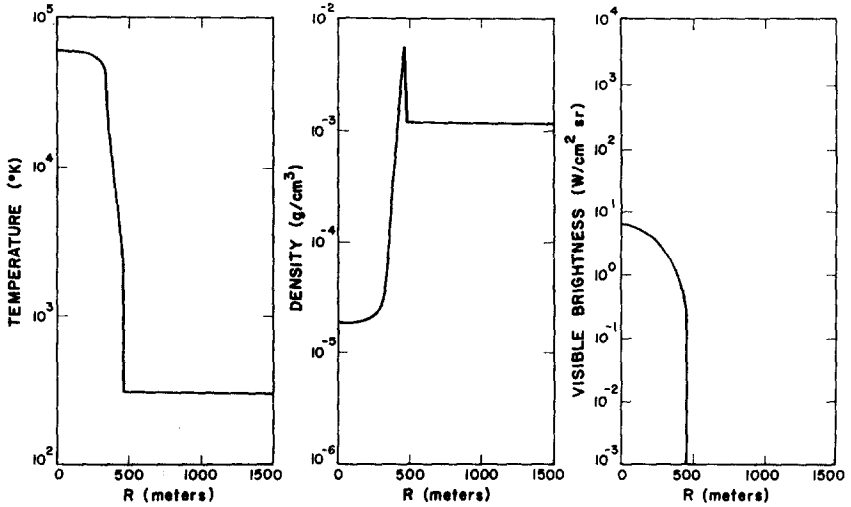

FIG. 7. Profiles of temperature, density, and visible brightness for $t = 9 \times 10^{-2}$ sec.

The fireball continues to expand behind the increasingly transparent shock. Its intrinsic brightness decreases with time, but its surface area increases, producing, for a time, a steady increase in radiant power. The radiant power increases until transport within the fireball can no longer replenish the radiation losses from the surface. The system responds with the formation of a radiative "cooling wave," whose effect is to lower the temperature at the fireball surface and reduce its capacity to radiate [3, 6]. The process evolves as an inward-moving wave which drops the temperature to about 8000 K. The cooling wave arrests the accelerating radiation loss rate, which then passes over a maximum and drops off. Fireball profiles at the time of maximum (0.8 sec) are shown in Fig. 8. Shortly after the maximum the fireball becomes transparent.

Measured optical power vs time curves for sea level nuclear explosions have the characteristic shape of the computed curve in Fig. 6 [7]. The time of minimum power provides a measure of the yield.

The assumption of a discontinuous two-valued intensity vs θ distribution (Fig. 1) is based on the observed fact that a fireball appears as a sharply defined disc of

fairly uniform brightness, as illustrated by the computed brightness profiles in Figs. 3–5, 7, and 8.

The early portion of the computed power vs time curve (Fig. 6) shows a series of bothersome oscillations. These arise from inadequate spatial resolution of the fireball temperature profiles, such that in the computational mesh there is an abrupt transition between optically thin cells ($\tau \ll 1$) and thick cells ($\tau \gg 1$).

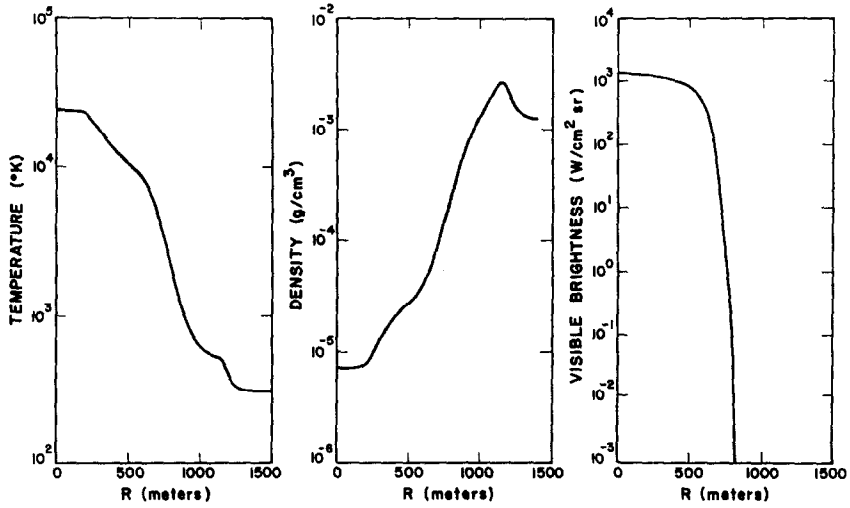

FIG. 8. Profiles of temperature, density, and visible brightness for $t = 0.8$ sec.

Owing to the rapid increase of optical absorption coefficients with increasing temperature, and the still more rapid increase of emission coefficients (μB), the emitted radiation tends, for practical purposes, to be produced in the outermost thick cell and attenuated in the next few cells. The primary role of a cell in this transition region changes from one of absorption to one of emission within 10–100 time steps. The output power goes through one cycle of an oscillation in the same period of time.

The oscillation problem could be solved in principle by the use of very thin mesh cells near the fireball front; however, attempts to implement this in practice have not been successful. Separate calculations [12] have shown that the radiance-determining layer in a high velocity shock front is of order 0.01 to 0.1 cm in thickness, and it has been impractical to use mesh cells of this size in fireball computations. (The difficulty comes mainly from the fact that the computational time step is tied to the minimum cell size via the Courant condition.)

The structures of shock fronts in the computations are determined artificially by

the viscous pressure Q [Eqs. (42)–(44)], and computed fireball radiance values are normally influenced by the shock structures. Errors are reduced by the device of setting the absorption coefficients in the artificial toe of a shock wave to the prevailing values ahead of the toe [13]. The result is that absorption of radiation in the toe is eliminated, and computed shock brightnesses are close to blackbody radiance values for the computed shock temperatures.

This computation, using 150 mesh cells and 40 frequency groups, required 20 min of CDC 7600 machine time.

Comparison with S_n Method

The computer code, known as RADFLO, embodies the present radiation transport scheme in the form of a subroutine. An alternative radiative transport subroutine using an S_n method has been constructed recently by Reed and Horak [14, 15]. It is possible, therefore, to compare results of a normal RADFLO calculation and several S_n-RADFLO calculations of the same problem with different values of n (i.e., different numbers of streams).

The test problem chosen was similar to the problem just described. Comparison of the several sets of computed results for the test problem led to the following conclusions:

(1) In the early phase of the problem, ($t \leqslant 10^{-3}$ sec) accuracy of the S_n calculations improved with increasing n up to S_8 (8 streams). Further increase of n beyond 8 had no effect. After 10^{-3} sec all of the S_n calculations ($2 \leqslant n \leqslant 8$) gave the same result.

(2) During the X-ray deposition phase of the problem ($t \leqslant 10^{-7}$ sec) the standard RADFLO result was the same as the S_8 result. (During this phase the source radius R_s in the RADFLO scheme is set equal to the radius of the central cell.)

(3) During the radiative expansion phase ($10^{-7} \leqslant t \leqslant 10^{-4}$ sec) the S_8 fireball grows about 10% faster than the RADFLO fireball. At the end of the radiative expansion phase the temperature gradient at the S_8 fireball surface is less steep, and the air shock develops somewhat more gradually. The S_8 result is probably the more accurate.

(4) However, for $t < 10^{-3}$ sec the S_8 and RADFLO radiant power vs time curves exhibit similar oscillations, due to the effects of inadequate spatial resolution and viscous pressure. Neither scheme gives physically valid results in this time interval. After 10^{-3} sec, differences between the S_2, S_4, S_8, and RADFLO results disappear.

(5) An S_8 transport cycle involves about four times as many computer operations as a RADFLO cycle.

Possible Astrophysical Applications

The present computer code has possible applications in astrophysical fireball problems—e.g. in supernova explosions. It is, however, limited in its ability to treat radiation transport in spectral lines, and it has no provision for treatment of scattering. The S_n scheme is probably preferable for such problems [14].

Summary

The difference scheme described in this paper has the primary virtue of simplicity. The approximations used for the angular distribution of intensity are realistic for problems in which the optical absorption coefficients have a wide range of values within the physical system, and they are also accurate for systems which are optically thick or thin.

Major inaccuracies arise from the groupwise averaging of absorption coefficients, as well as from uncertainties in the coefficients themselves. Other errors arise from inadequate spatial resolution of the temperature profiles in expanding fronts. The simplicity and speed of the present radiation transport scheme permits the greatest amount of computational detail to be devoted to spectral and spatial resolution, where it is most needed.

Acknowledgments

I am indebted to John W. Kodis for major contributions to maintenance and development of the present RADFLO code. Other major contributions have been made by D. S. Sappenfield and F. E. Fajen. I am also grateful to H. G. Horak for his efforts in designing the S_n radiation transport program and for furnishing the comparisons between S_n and RADFLO. This work was performed under the auspices of the U. S. Atomic Energy Commission.

References

1. R. D. Richtmeyer and K. W. Morton, "Difference Methods for Initial Value Problems," 2nd ed., Tracts in Mathematics No. 4, Interscience Publishers, New York, 1967.
2. H. A. Bethe, Blast Wave, Los Alamos Scientific Laboratory Report LA-2000, August 1947.
3. H. A. Bethe, Theory of the Fireball, Los Alamos Scientific Laboratory Report LA-3064, February 1964.

4. H. L. BRODE, Review of nuclear weapons effects, *Ann. Rev. Nucl. Sci.* **18** (1968), 153–202.
5. R. W. HILLENDAHL, Theoretical Models for Nuclear Fireballs, DASA-1589 Part A (Lockheed Missiles & Space Co., LMSC-B006750), August 1965.
6. YA. B. ZEL'DOVICH, A. S. KOMPANEETS, AND YU. P. RAIZER, *JETP* **7** (1958), 882 and 1001 (English translation).
7. S. GLASSTONE, Ed., "The Effects of Nuclear Weapons," Rev. ed., U.S. Dept. Defense, USAEC, April 1962.
8. J. HILSENRATH, M. S. GREEN, AND C. W. BECKETT, Thermodynamic Properties of Highly Ionized Air, Air Force Special Weapons Center, AFSWC-TR-65-35, April 1957.
9. J. HILSENRATH AND M. KLEIN, "Tables of Thermodynamic Properties of Air in Chemical Equilibrium Including Second Virial Corrections from 1500° K to 15,000° K," Arnold Engineering Development Center, Air Force Systems Command, AEDC-TDR-63-161, August 1963.
10. D. R. CHURCHILL, B. H. ARMSTRONG, R. R. JOHNSTON, AND K. G. MULLER, "Absorption Coefficients of Heated Air: A Tabulation to 24,000° K," *J. Quant. Spectrosc. Radiat. Transfer* **6** (1966), 371–422.
11. A. N. COX AND J. N. STEWART, "Radiative and Conductive Opacities and Monochromatic Absorption Coefficients of Air," Los Alamos Scientific Laboratory Report LAMS-3014, September 1962.
12. J. ZINN AND R. C. ANDERSON, "On the Structure and Brightness of Strong Shock Waves in Air," submitted for publication in *Phys. Fluids.*
13. This procedure was invented by R. W. Hillendahl, private communication.
14. H. G. HORAK, Los Alamos Scientific Laboratory, private communication.
15. K. D. LATHROP AND B. G. CARLSON, Numerical solution of the Boltzmann equation, *J. Comp. Phys.* **1** (1966), 173.